

DOI: 10.1002/((please add manuscript number))

Article type: Communication

Biom mineralization as a paradigm of directional solidification: A physical model for molluscan shells ultrastructural morphogenesis

*Vanessa Schoeppler[#], László Gránásy[#], Elke Reich, Nicole Poulsen, René de Kloe, Phil Cook, Alexander Rack, Tamás Pusztai, Igor Zlotnikov**

Dr. V. Schoeppler[#], Dr. E. Reich, Dr. N. Poulsen, Dr. I. Zlotnikov*
B CUBE – Center for Molecular Bioengineering, Technische Universität Dresden, Germany
E-mail: igor.zlotnikov@tu-dresden.de

Dr. R. de Kloe
EDAX, Tilburg, The Netherlands

Dr. P. Cook, Dr. A. Rack
ESRF – The European Synchrotron, Grenoble, France

Prof. L. Gránásy[#], Dr. T. Pusztai
Institute for Solid State Physics and Optics, Wigner Research Centre for Physics, Budapest, Hungary

[#]These authors contributed equally to this work

Keywords: biomineralization, crystal growth, solidification, mollusc shells, phase-field modeling

Abstract: Molluscan shells are a model system to understand the fundamental principles of mineral formation by living organisms. The diversity of unconventional mineral morphologies and three-dimensional mineral-organic architectures that comprise these tissues, in combination with their exceptional mechanical efficiency, offers a unique platform to study the form-structure-function relationship in a biomineralized system. However, so far, morphogenesis of these ultrastructures is poorly understood. Here, we develop a comprehensive physical model, based on the concept of directional solidification to describe molluscan shell biomineralization. Using the shell of *Unio pictorum*, we demonstrate its capacity to formulate the process of morphogenesis of the entire shell construct – the prismatic and the nacreous ultrastructures and their transitions, and to define the forces and thermodynamic constraints that govern the evolution of the constituting mineralized assemblies on ultrastructural and nanostructural levels. Thereby, we provide explicit tools for novel bioinspired and biomimetic bottom-up materials design.

The formation of three-dimensional mineral-organic functional architectures by living organisms is a tremendously active research field spanning many scientific disciplines^[1–3]. Classically, the topic of biomineralization was primarily the focus of earth sciences. Later, it gained the attention of researchers from different branches in chemistry and biology and currently, it is one of the most exciting topics in materials science. The cross-disciplinary interest in biomineralization stems from the efficiency of the biochemical machinery that is responsible for bottom-up biotic mineral formation, functional capacity of the mineralized

tissue as a whole and, at the same time, elegance and even simplicity of the solutions it provides to the organisms. These are the main goals of current human technology.

Mollusc shells biomineralization is an exemplar system to study the process of biogenic calcium carbonate (CaCO_3) formation. First appearing during the Ediacaran, more than 500 million years ago, molluscs have developed hard and stiff mineralized outer shells for structural support and protection against predation^[4]. These shells consist of intricate mineral-organic composite ultrastructures made of calcium carbonates, predominately calcite and aragonite. The different ultrastructures are arranged in layers parallel to the outer surface of the shell and are usually separated by an organic membrane, each layer having a distinct 3D morphology and shape of the comprising mineral building blocks^[5]. For example, the calcitic prismatic ultrastructure in bivalves consists of elongated mineral columns glued together by an organic phase and the aragonitic nacreous ultrastructure is made of platelets surrounded by a relatively thin organic matrix^[6]. During the last few decades, significant progress has been made in understanding the key biochemical mechanisms responsible for biotic CaCO_3 formation – its polymorph selection and pathways towards nucleation and growth^[7–11]. However, the topic of morphogenesis of shells on the ultrastructural level was largely neglected and only a few models describing the formation of nacre exist^[12–16].

Recent studies show that the formation of different shell ultrastructures is the result of a thermodynamically driven self-assembly processes. The control over the shape of the individual mineral building blocks and the morphology of the entire composite assembly was suggested to be exerted by the organisms by adjusting the necessary physical and chemical environment in which the different mineral architectures grow spontaneously in accordance with these boundary conditions^[6,17,18]. The rationale behind this assertion is the fact that the mineral phase is formed unidirectionally on an organic periostracal layer by the inner soft tissue of molluscs (epithelial cells of the mantle tissue) extracellularly. The growth proceeds in a liquid filled cavity (the extrapallial space) between the mantle tissue and the biomineralizing front^[19]. Hence, the cells do not have a direct control over mineral formation but choreograph the process remotely by, for example, secreting the necessary inorganic precursors and organic framework, controlling their saturation levels in the growth medium and setting the necessary pH level and viscosity. In fact, the process of shell formation is reminiscent of technologically relevant materials synthesis methods well known from the fields of materials science and colloid chemistry. Specifically, directional solidification of alloys and colloidal suspensions.

In this study, using the shell of the freshwater mussel *Unio pictorum* as a model and phase-field simulation as computational support, we demonstrate that the biomineralization of this mollusc shell is a paradigm of directional solidification. We show that the entire shell construct, comprising a number of layers with different morphologies, is the result of a continuous growth process with gradually changing boundary conditions. Using analogies to well-studied systems from classic materials science, we provide the basis for understanding the physical constraints governing the morphogenesis of shell ultrastructures, thereby explaining the limited variety of architectures observed in different molluscan clades, and develop a novel comprehensive approach to understand and mimic mineral formation by living organisms.

The entire shell of *U. pictorum* (**Figure 1A**) is aragonitic^[20] (Figure S1). The shell grows in thickness unidirectionally towards the inner part of the animal. SEM imaging of a polished cross-section of the shell (Figure 1B) demonstrates the first seemingly prismatic and the second nacreous two-layer architecture (sheet nacre^[6,13]), well-known for species of the Unionidae family^[21] and other molluscs^[22]. Due to the columnar shape of the mineral units in the bottom layer in Figure 1B, it was previously classified as a simple prismatic

ultrastructure^[23]. The upper layer in Figure 1B shows a lamellar arrangement of 1 μm thick platelets, typical for sheet nacre ultrastructures. A cryo-fractured cross-section of the shell shows that the mineral blocks are composed of sub-100 nm sized granules that gradually change their packing behavior from the prismatic layer to nacre (Figures 1C-1F). Similar to other Unionidae species^[21], during the initial stages of prism formation, close to the periostracum, these nanogranules are randomly aggregated (Figure 1C). As the prisms develop, the granules start to form dense elongated structures co-aligned with the direction of growth (Figure 1D). Close to the nacre, these structures thicken and transition into thick fibers (Figure 1E) that become transversely segmented while they gradually segue into nacre platelets (Figure 1F). In nacre, the nanoparticle assembly process reaches a steady state where they aggregate to form a well-defined platelet structure throughout the rest of the shell.

The morphology of the prismatic ultrastructure in 3D was studied by employing absorption- and phase-contrast enhanced microtomography at beamline ID19 of the European Synchrotron Radiation Facility (ESRF). The organic interprismatic boundaries were easily resolved using spatial sampling of 0.162 μm . Two-dimensional binarized tomographic sections, one closer to periostracum and one closer to nacre, obtained perpendicular to the growth direction of the shell, are presented in **Figure 2A** and **2B**, respectively. Here, the mineral and the organic components correspond to white and black areas, respectively. Surprisingly, whereas, adjacent to nacre, the prisms appear as isolated polygons separated by the organic interprismatic matrix (Figure 2B) – a morphology that is commonly observed in simple prismatic structures^[6,17], in proximity to the periostracum, the mineral units exhibit a dendritic morphology (Figure 2A). A disordered dendritic prismatic structure in shells was never previously reported. Representative 3D tomographic reconstructions at different stages of prismatic layer formation, showing a gradual transition from the dendritic to the prismatic morphology, are presented in Figures 2C-2E. During the initial stages of shell biomineralization, the mineral units have a classic dendritic morphology (Figure 2C). Then, the dendrites morph to appear as a simple prismatic ultrastructure (Figure 2D). Finally, the growth of the prisms proceeds in a columnar mode where bigger prisms coarsen at the expense of shrinking smaller ones^[17] (Figure 2E). The variation in aragonite particles packing and mineral blocks morphology is reflected in local mechanical properties of the shell measured on a cross-section parallel to the growth direction using nanoindentation (Figure 1G). The reduced modulus of 9.8 ± 0.7 GPa and hardness of 0.4 ± 0.05 GPa in the dendritic zone are relatively small and are comparable to the properties to the purely organic periostracum in its dry state (Figure 1H and Figure 1I, respectively). In the columnar area, where the aragonitic particles are densely packed, the mechanical properties abruptly increase to reduced modulus of 60.1 ± 12.3 GPa and hardness of 2.8 ± 1.2 GPa and become comparable to previously reported properties of biogenic aragonite^[5]. These values do not change throughout the rest of the shell.

Transformation of aragonitic particle packing, on the nanoscale, and of the morphology of the architecture, on the macroscale, is also accompanied by a gradual transition of the crystallographic arrangement of the particles. Electron back-scattered diffraction (EBSD) analysis of a cross-section of the shell prepared parallel to its growth direction is presented in **Figure 3A** and **Figure 3B**. In contrast to calcitic prismatic architectures^[24], aragonitic nanoparticles comprising the dendritic and the prismatic ultrastructures in *U. pictorum* show no preferred orientation and no monocrystalline characteristics. Texturing appears just before the transition to nacre with the formation of coherent fibrous units (Figure 1E and Figure 1F), with the *c*-axis of aragonite parallel to the growth direction of the shell (Figure 3A). This preferred orientation is maintained with the gradual transition into the nacreous ultrastructure and thereafter, which is in agreement with previous studies of the crystallographic nature of nacre^[25,26]. This observation is supported by synchrotron-based x-ray diffraction

measurements, performed at ID06 at the ESRF. Using a rectangular incident beam of $600 \times 20 \mu\text{m}^2$, diffraction patterns were collected at different positions along the shell with the long side of the rectangle perpendicular to the growth direction of the shell (pattern indexing is presented in Figure S1). These positions are also indicated by dashed lines in Figure 3A. In the dendritic zone (Figure 3C), the obtained ring-like diffraction pattern confirms the absence of texture in that area. Some preferred orientation becomes apparent when measuring at the center of the prismatic area (Figure 3D), probably due to the appearance of fibers at the edges of the prisms (Figure 3A). At the transition to nacre (Figure 3E), a pronounced texture is developed where the *c*-axis of aragonite is co-aligned with the growth direction of the shell. Similar high degree of preferred orientation is continued to the nacreous ultrastructure (Figure 3F). Both techniques, EBSD and x-ray diffraction analysis, clearly demonstrate that the crystallographic orientation of nacre tablets is inherited from the fibers in the prisms^[15,16].

Morphological, structural and crystallographic analyses of the shell of *U. pictorum* demonstrate continuous directional formation of the entire shell construct accompanied by an increasing degree of order. In fact, the process of ordering occurs on two hierarchical levels. On the ultrastructural level, the transition proceeds from a dendritic via more regular prismatic into the highly ordered nacreous structure. On the level of the nanostructure, a progressive increase in nanoparticle alignment and texturing are achieved. On both hierarchical levels, the transitions occur gradually undoubtedly indicating a common growth mechanism reminiscent of microstructural evolution of materials obtained via different directional solidification processes.

Directional solidification is a broadly studied topic in materials science with a high technological importance. Solidification from a liquid or a gaseous phase can result in polycrystalline structures with a remarkable variety of morphologies and three-dimensional assemblies. The patterns are determined by the interplay of capillarity and diffusion, phenomena influenced by temperature and/or supersaturation, which also determine the thermodynamic driving force for crystallization^[27,28]. At low thermodynamic driving force, or near equilibrium condition, the solidification process results in symmetric single crystals, whereas a high thermodynamic force leads to the formation of disordered polycrystalline dendrites and spherulitic structures^[29]. The most commonly studied solidifying systems are metals, alloys, polymer systems, colloidal suspensions, and water. For example, a large variety of ice crystal morphologies, such as dendrites, needles, platelets and columns, can be obtained by simply changing the temperature and supersaturation of the water vapor phase^[30]. In the case of colloidal suspensions, a variety of ultrastructures, such as dendritic, equiaxed, columnar and layered (banded) morphologies have been shown to arise from clay and silica dispersed in water by changing the temperature gradient during freeze casting^[31,32]. In fact, directional solidification is usually realized by introducing a temperature gradient or spatial variation of the concentration in the solidifying system that influence the direction and growth velocity of the solidification. Moreover, variation of the thermodynamic driving force/velocity along this direction can lead to a transition from one morphology to another without changing the chemistry of the system. For example, a transition from a regular lamellar to banded structure is observed in a number of dendritic and eutectic alloys, with increasing velocity of the solidifying front^[33], a transition from a planar to columnar to dendritic morphology is observed in alloys, when the solidification velocity is increased^[34] and a transition from a planar to dendritic morphology is observed in polymeric systems, when increasing the driving force^[29,35]. The velocity of the solid-liquid interface not only influences the morphology of the solid but also has a considerable effect on growth kinetics and therefore, the microstructure of the solid. In a broad range of systems, the “fast” growth mode that is the consequence of a high thermodynamic driving force, was shown to result in

the formation of disordered polycrystalline structures. In contrast, the “slow” growth mode, occurring at low driving forces, leads to the formation of near-equilibrium single-crystals^[29].

During shell biomineralization, three main component types are secreted into the extrapallial space and participate in the process of solidification: amorphous calcium carbonate (ACC)^[36,37], the insoluble organic fraction consisting mainly of β -chitin and related chitin binding proteins^[10,13,38] and the soluble organic fraction largely made of proteins^[7,9,39,40]. The latter component was shown to be primarily responsible for ACC stabilization, calcium carbonate polymorph selection (calcite or aragonite) and for effecting the equilibrium shape of the mineral units^[7,9,11,40]; however, it does not undergo crystallization but is incorporated into the growing structure^[41]. In contrast, ACC and β -chitin are two crystalizing components that are key to the morphological evolution of the growing shell construct. Recent evidence suggests that mineral unit formation proceeds via colloidal attachment of ACC nanoparticles, up to 100 nm in diameter, followed by crystallization and fusion with the growing crystal^[36,42,43]. Whereas, disordered β -chitin was shown to be present in prismatic ultrastructures^[38,44], its crystalline form plays a crucial role in the formation of the nacreous architecture^[13,45]. It is postulated that the organic membranes between the mineral layers in nacre are composed of β -chitin nanocrystallites, which self-assemble into a layered liquid crystalline structure ahead of the solidifying front. In turn, aragonite is formed between the organic membranes forming a periodic mineral-organic layered structure known as sheet nacre^[13].

Based on this knowledge, we suggest a model for the formation of the shell in *U. pictorum*. The behaviors and morphologies obtained during directional solidification well describe the structural evolution of the shell of the entire *U. pictorum* shell construct, at the ultrastructural and the nanostructural levels. Random aggregation of aragonitic nanoparticles (Figure 1C and Figure 3C) and the dendritic morphology during the initial stages of shell deposition (Figure 2C) indicate a relatively fast growth mode. The realization by the organism seems relatively simple, by providing a high ACC concentration. A fast growth mode appears also reasonable at an early stage of shell development, since it would quickly provide the organism with a first protective barrier. Progressive texturing of aragonite on the nanostructural level (Figure 1 and Figure 3) suggests a deceleration of the growth front velocity. In analogy to classic materials, such as alloys^[46], organic materials^[47] and colloidal suspensions^[31], the dendritic prisms in *U. pictorum* are oriented parallel to the growth direction of the shell (Figure 1B and Figure 2E). The aragonitic particles co-align to form elongated fibers that form the prisms (Figure 1E and Figure 3E) and the insoluble organic fraction is incorporated in the structure or being displaced to form the interprismatic organic matrix (Figure S2). Finally, the nacreous ultrastructure appears, initially having a non-uniform morphology and later extremely regular layered characteristics (Figure 1B and Figure 3A). Here, shell formation reaches a steady state regime and the velocity of the solidifying front is sufficiently decreased allowing chitin to crystallize ahead of the solidification front and thus, to shape the nacreous architecture in accordance with the formerly suggested mechanism^[13]. Previously, banded structures were reported to appear in alloys^[33,48] and colloidal suspensions^[31,32] as a result of directional solidification of two different crystalizing phases at relatively slow velocities that represent a steady-state growth^[28,49,50]. When the two phases exhibit different crystallization kinetics and thermodynamics, one phase can crystallize ahead of the other and block its planar and stable growth. In the case of *U. pictorum*, these phases are calcium carbonate and β -chitin. Theoretically, the growth process described above could be maintained by the mantle cells by adjusting the concentration level of the mineral phase or both the mineral and β -chitin in the extrapallial space.

To support the proposed model, we performed two-dimensional simulations of structural evolution during the solidification of the shell within the framework of a phase-field model

that was previously successfully employed to describe complex polycrystalline morphologies^[29,51,52]. The local state of the matter is described by three fields: the phase-field that monitors crystallization (Movie S1), the concentration field that represents the local molar fraction of calcium carbonate (**Figure 4A**, Movie S2), and the orientation field, which monitors the local crystallographic orientation (Figure 4B, Movie S3). In all the simulations, the solidifying front propagated from the bottom of the images upward. The solidifying system was regarded as a quasi-binary solution, in which the extrapallial fluid is viewed as a solution of calcium carbonate and an organic component. In compliance with the suggested model, it was assumed that the supersaturation of calcium carbonate – the driving force of solidification – decreases exponentially during the solidification process (Figure S3). The concentration map (Figure 4A) demonstrates the formation of two distinct ultrastructures (columnar and banded – the prismatic layer and nacre) and the gradual transition between the two (compare to Figure 1B). Here, the darker interfacial layers indicate a high concentration of the organic component. On the nanostructural level, the orientation distribution field (Figure 4B) qualitatively reproduces the initial solidification of randomly oriented small crystallites that transition into thick fibrous domains in the prismatic region, which seed the crystallographic nature of nacre (compare to Figure 3A). Clearly, a remarkable resemblance to the shell of *U. pictorum* was obtained on both, ultrastructural and nanostructural levels.

In this work, directional solidification is used to describe the morphogenesis of the aragonitic shell in *U. Pictorum*. However, the presented concepts are comprehensive and can be applied to describe the evolution of continuous shell architectures in many other species, such as the transition from equiaxed morphology to prismatic to columnar nacre that is observed in aragonitic shells of *Nautilus pompilius* and *Haliotis asinina*^[53]. Moreover, they can be applied to describe the formation of individual ultrastructural layers, such as the nacre of *Pinna nobilis* that shows a transition from disordered packing of aragonitic particles that gradually transform to an ordered layered structure^[54]. Certainly, each example must be individually examined; however, in all cases, a similar trend is observed: a transition from a fast to slow directional solidification mechanism, accompanied by increased morphological regularity. Whereas the process of molluscan shells biomineralization is clearly under strong genetic control, the proposed model describes how this control is executed on the level of the ultrastructure – by setting the biochemical and physical conditions necessary for a specific morphology to self-assemble. In particular, the model demonstrates how the cells can form complex multifunctional structures by simply controlling the chemical environment and transport to the extracellular space. It is astonishing that processes from classic materials science have the capacity to describe the formation of a complex biomineralized tissue created by a living organism. The analogy to well-studied processes from materials science provides us with quantitative analytical tools and a unique opportunity to assess these boundary conditions and to apply this knowledge in bioinspired bottom-up materials design.

Experimental Section

Sample preparation: For environmental scanning electron microscopy and nanoindentation, samples of the shell of the bivalve *Unio pictorum* were fractured, embedded in PMMA, cut parallel to the direction of growth and diamond polished. Electron back-scattered diffraction analysis required additional polishing with colloidal silica. For fracture analysis, shell fragments were cryo-fractured via freezing with liquid nitrogen and subsequent manual fracturing. For microtomography, a shell fragment was ground into a 2 mm long cylinder with a diameter of approximately 1 mm. The long axis of the cylinder corresponded to the growth direction. The cylinder was glued onto the sample holder with the cylinder long axis co-aligned with the rotation axis of the sample holder stage, perpendicular to the incident x-ray beam. For x-ray diffraction analysis, a rectangular sample with a length of approximately 2 mm and a width of approximately 350 μm was prepared. The sample was glued onto the sample holder with the long axis co-aligned with the rotation axis of the sample holder stage, perpendicular to the incident x-ray beam.

Electron microscopy and electron back-scattered diffraction analysis: The polished cross-section was imaged using the environmental scanning electron microscope FEI FE-ESEM, Quanta 600 in low vacuum mode. The cryo-fractured sample was coated with chromium and imaged using a Scios Dual Beam FIB/SEM (FEI) in high vacuum conditions. EBSD data were collected using an EDAX Hikari Super EBSD system on a FEI Quanta 250feg SEM using 12kV, 800 pA beam conditions to minimize damage to the specimen. During the data acquisition all EBSD patterns were recorded which allowed off-line NPAR reprocessing to optimize the indexing success^[55].

Mechanical characterization: Nanoindentation experiment was performed using a Berkovich diamond tip in Triboscan 950 (Hysitron). A load function consisting of 5 seconds loading segment, 5 seconds holding segment at a maximal load of 1000 μN and 5 seconds unloading segment was used to characterize the surface of the sample that was cut perpendicular to the growth direction of the shell. 2D maps of reduced modulus and hardness were obtained by performing 225 indents with an interval of 3.5 μm – 15 \times 15 indents. The values were calculated using the standard Oliver-Pharr approach.

Microtomography: To visualize the 3D spatial arrangement of the dendritic-prismatic ultrastructure, synchrotron-based microtomography was performed on the beamline ID19 at the European Synchrotron Radiation Facility (ESRF) in Grenoble (France). The shell was scanned using an x-ray photon energy of 19 keV and a sample-detector distance of 8 mm. A total of 5000 radiographic projection images were recorded over 180 degrees with an exposure time of 0.1 s and an effective pixel size of 0.162 μm . An ESRF in-house code (PyHST2) was used to reconstruct the data. Prism boundaries were enhanced by means of Paganin-based filtering with a delta/beta ratio of 50. 3D segmentation and visualization was performed using Avizo (FEI Visualization Science Group).

X-ray diffraction analysis: X-ray diffraction analysis was carried out on the ID06 beamline at the ESRF in Grenoble (France). The sample was illuminated with a beam of 17 keV. Using slits, the beam was restricted to a size of 600 \times 20 μm^2 . The sample was mounted with the growth axis perpendicular to the wide axis of the x-ray beam. The sample was scanned over 500 μm along the growth axis in 10 μm steps. Diffraction images were recorded using a FReLoN camera (ESRF, Atmel TH7899 charge-coupled device sensor chip, 2048 \times 2048 pixels, 16 bit) bonded to a fiber optic taper with a scintillator (47.5 \times 47.5 μm^2 pixel size). The camera was mounted 188 mm behind the sample and exposure time was 1 sec/frame.

Phase-field modeling: The equations of motion were solved in a dimensionless form numerically on a rectangular grid of size 3000 \times 2000 employing an in-house code, using finite difference discretization with a forward Euler time stepping and parallel computing. The computations were performed on a CPU cluster consisting of 608 CPU cores in three blocks. For the sake of simplicity, in our qualitative simulations ideal solution thermodynamics was

used^[56]. The most important model parameters used here were as follows: phase-field mobility was chosen as $m_{\phi,0} = 0.9$, while the orientation mobility was taken as $m_{\theta,l} = 120$. We assumed a $k = 4$ -fold anisotropy of the interfacial free energy $s = 1 + (s_0/2) \cos[k(\mathcal{G} - 2\pi\theta/k)]$, where $s_0 = 0.04$ is the strength of the anisotropy, $\mathcal{G} = \text{atan}[(\nabla\phi)_y/(\nabla\phi)_x]$ the direction of the normal of the solid-liquid interface, $(\nabla\phi)_y$ and $(\nabla\phi)_x$ the y and x components of the gradient of the phase field. In our computations no kinetic anisotropy was assumed ($\delta_0 = 0$). The model parameters not specified here were chosen as described in a previous study^[51].

Supporting Information

Supporting Information is available from the Wiley Online Library or from the author.

Acknowledgements

I.Z. acknowledges the financial support provided by Bundesministerium für Bildung und Forschung (BMBF) through grant 03Z22EN11. L.G. acknowledges the support provided by the National Research, Development, and Innovation Office (NKFIH), Hungary under contracts K-115959 and KKP-126749. We thank Dr. Carsten Detlefs (ESRF), Dr. Can Yildirim (ESRF) and Dr. Anders C. Jakobsen (Danish Technical University) for their support on ID06. We acknowledge the European Synchrotron Radiation Facility for beamtime allocation on beamlines ID19 and ID06. This work was supported by the Light Microscopy Facility, a core facility of CMCB at Technische Universität Dresden.

References

- [1] S. Weiner, P. M. Dove, *Rev. Mineral. Geochemistry* **2003**, *54*, 1.
- [2] H. A. Lowenstam, S. Weiner, *On Biomineralization*, Oxford University Press, New York, **1989**.
- [3] S. Mann, *Biomineralization*, Oxford University Press, New York, **2001**.
- [4] J. Vinther, *Palaeontology* **2015**, *58*, 19.
- [5] J. D. Currey, J. D. Taylor, *J. Zool.* **1974**, *173*, 395.
- [6] I. Zlotnikov, V. Schoeppler, *Adv. Funct. Mater.* **2017**, *1700506*, 1700506.
- [7] G. Falini, S. Albeck, S. Weiner, L. Addadi, *Science* **1996**, *271*, 67.
- [8] S. Weiner, L. Addadi, *Trends Biochem. Sci.* **1991**, *16*, 252.
- [9] M. Suzuki, K. Saruwatari, T. Kogure, Y. Yamamoto, T. Nishimura, T. Kato, H. Nagasawa, *Science* **2009**, *325*, 1388.
- [10] M. Suzuki, H. Nagasawa, *Can. J. Zool.* **2013**, *91*, 349.
- [11] R. A. Metzler, J. S. Evans, C. E. Killian, D. Zhou, T. H. Churchill, N. P. Appathurai, S. N. Coppersmith, P. U. P. A. Gilbert, *J. Am. Chem. Soc.* **2010**, *132*, 6329.
- [12] F. Nudelman, *Semin. Cell Dev. Biol.* **2015**, *46*, 2.
- [13] J. H. E. Cartwright, A. G. Checa, *J. R. Soc. Interface* **2007**, *4*, 491.
- [14] I. C. Olson, A. Z. Blonsky, N. Tamura, M. Kunz, B. Pokroy, C. P. Romao, M. A. White, P. U. P. A. Gilbert, *J. Struct. Biol.* **2013**, *184*, 454.
- [15] A. G. Checa, J. H. E. Cartwright, M. G. Willinger, *J. Struct. Biol.* **2011**, *176*, 330.
- [16] T. E. Schäffer, C. Ionescu-Zanetti, R. Proksch, M. Fritz, D. A. Walters, N. Almqvist, C. M. Zaremba, A. M. Belcher, B. L. Smith, G. D. Stucky, D. E. Morse, P. K. Hansma, *Chem. Mater.* **1997**, *9*, 1731.
- [17] B. Bayerlein, P. Zaslansky, Y. Dauphin, A. Rack, P. Fratzl, I. Zlotnikov, *Nat. Mater.* **2014**, *13*, 1102.
- [18] D. Zöllner, E. Reich, I. Zlotnikov, *Cryst. Growth Des.* **2017**, *17*, 5023.
- [19] F. Marin, N. Le Roy, B. Marie, *Front. Biosci.* **2012**, *S4*, 1099.
- [20] J. D. Taylor, W. J. Kennedy, A. Hall, *Bull. Brit. Mus.* **1969**, *3*, 1.
- [21] A. G. Checa, A. Rodriguez-Navarro, *Proc. R. Soc. B Biol. Sci.* **2001**, *268*, 771.
- [22] Y. Dauphin, G. Luquet, M. Salome, L. Bellot-Gurlet, J. P. Cuif, *J. Microsc.* **2018**, *270*, 156.
- [23] S. V. Popov, *Paleontol. J.* **2014**, *48*, 1519.
- [24] I. C. Olson, R. A. Metzler, N. Tamura, M. Kunz, C. E. Killian, P. U. P. A. Gilbert, *J. Struct. Biol.* **2013**, *183*, 180.
- [25] B. J. Maier, E. Griesshaber, P. Alexa, A. Ziegler, H. S. Ubhi, W. W. Schmahl, *Acta Biomater.* **2014**, *10*, 3866.
- [26] E. Griesshaber, W. W. Schmahl, H. Singh, J. Huber, F. Nindiyasari, B. Maier, A. Ziegler, *Acta Biomater.* **2013**, *9*, 9492.
- [27] G. Coquerel, *Chem. Soc. Rev.* **2014**, *43*, 2286.
- [28] J.-J. Xu, *Interfacial Wave Theory of Pattern Formation in Solidification*, Springer International Publishing, Cham, **2017**.
- [29] L. Gránásy, T. Pusztai, T. Börzsönyi, J. A. Warren, J. F. Douglas, *Nat. Mater.* **2004**, *3*, 645.
- [30] K. G. Libbrecht, *Reports Prog. Phys.* **2005**, *68*, 855.
- [31] S. S. L. Peppin, J. a. W. Elliott, M. G. Worster, *J. Fluid Mech.* **2006**, *554*, 147.
- [32] J. M. H. Schollick, R. W. Style, A. Curran, J. S. Wettlaufer, E. R. Dufresne, P. B. Warren, K. P. Velikov, R. P. A. Dullens, D. G. A. L. Aarts, *J. Phys. Chem. B* **2016**, *120*, 3941.
- [33] M. Carrard, M. Gremaud, M. Zimmermann, W. Kurz, *Acta Met. Mater.* **1992**, *40*, 983.
- [34] Y. Chen, B. Billia, D. Z. Li, H. Nguyen-Thi, N. M. Xiao, A. A. Bogno, *Acta Mater.* **2014**, *66*, 219.

- [35] G. Tegze, L. Gránásy, G. I. Tóth, J. F. Douglas, T. Pusztai, *Soft Matter* **2011**, 7, 1789.
- [36] R. T. Devol, C. Y. Sun, M. A. Marcus, S. N. Coppersmith, S. C. B. Myneni, P. U. P. A. Gilbert, *J. Am. Chem. Soc.* **2015**, 137, 13325.
- [37] J. J. De Yoreo, P. U. P. A. Gilbert, N. A. J. M. Sommerdijk, R. L. Penn, S. Whitelam, D. Joester, H. Zhang, J. D. Rimer, A. Navrotsky, J. F. Banfield, A. F. Wallace, F. M. Michel, F. C. Meldrum, H. Cölfen, P. M. Dove, *Science* **2015**, 349.
- [38] S. Weiner, W. Traub, *FEBS Lett.* **1980**, 111, 311.
- [39] B. Marie, N. Guichard, J. P. De Barros, G. Luquet, F. Marin, *Biominer. from Paleontol. to Mater. Sci.* **2007**, 273.
- [40] A. M. Belcher, X. H. Wu, R. J. Christensen, P. K. Hansma, G. D. Stucky, D. E. Morse, *Nature* **1996**, 381, 56.
- [41] B. Marie, G. Luquet, J.-P. Pais De Barros, N. Guichard, S. Morel, G. Alcaraz, L. Bollache, F. Marin, *FEBS J.* **2007**, 274, 2933.
- [42] Y. Politi, J. Mahamid, H. Goldberg, S. Weiner, L. Addadi, *CrystEngComm* **2007**, 9, 1171.
- [43] C. Rodriguez-Navarro, A. Burgos Cara, K. Elert, C. V. Putnis, E. Ruiz-Agudo, *Cryst. Growth Des.* **2016**, 16, 1850.
- [44] F. Nudelman, H. H. Chen, H. A. Goldberg, S. Weiner, L. Addadi, *Faraday Discuss.* **2007**, 136, 9.
- [45] Y. Levi-Kalishman, G. Falini, L. Addadi, S. Weiner, *J. Struct. Biol.* **2001**, 135, 8.
- [46] M. Gündüz, E. Çadirli, *Mater. Sci. Eng. A* **2002**, 327, 167.
- [47] E. Üstün, E. Çadirli, H. Kaya, *J. Phys. Condens. Matter* **2006**, 18, 7825.
- [48] H. Yasuda, K. Tokieda, I. Ohnaka, *Mater. Trans.* **2000**, 41, 1005.
- [49] O. L. Rocha, C. A. Siqueira, A. Garcia, *Mater. Sci. Eng. A* **2003**, 347, 59.
- [50] W. Kurz, R. Trivedi, *Metall. Mater. Trans. A* **1996**, 27, 625.
- [51] L. Gránásy, T. Pusztai, G. Tegze, J. A. Warren, J. F. Douglas, *Phys. Rev. E - Stat. Nonlinear, Soft Matter Phys.* **2005**, 72, 1.
- [52] L. Gránásy, L. Rátkai, A. Szállás, B. Korbuly, G. I. Tóth, L. Környei, T. Pusztai, *Metall. Mater. Trans. A Phys. Metall. Mater. Sci.* **2014**, 45, 1694.
- [53] B. Marie, A. Marie, D. J. Jackson, L. Dubost, B. M. Degnan, C. Milet, F. Marin, *Proteome Sci.* **2010**, 8, 54.
- [54] R. Hovden, S. E. Wolf, M. E. Holtz, F. Marin, D. A. Muller, L. A. Estroff, *Nat. Commun.* **2015**, 6, 10097.
- [55] S. I. Wright, M. M. Nowell, S. P. Lindeman, P. P. Camus, M. De Graef, M. A. Jackson, *Ultramicroscopy* **2015**, 159, 81.
- [56] T. Pusztai, G. Tegze, G. I. Tóth, L. Környei, G. Bansel, Z. Fan, L. Gránásy, *J. Phys. Condens. Matter* **2008**, 20, 404205.

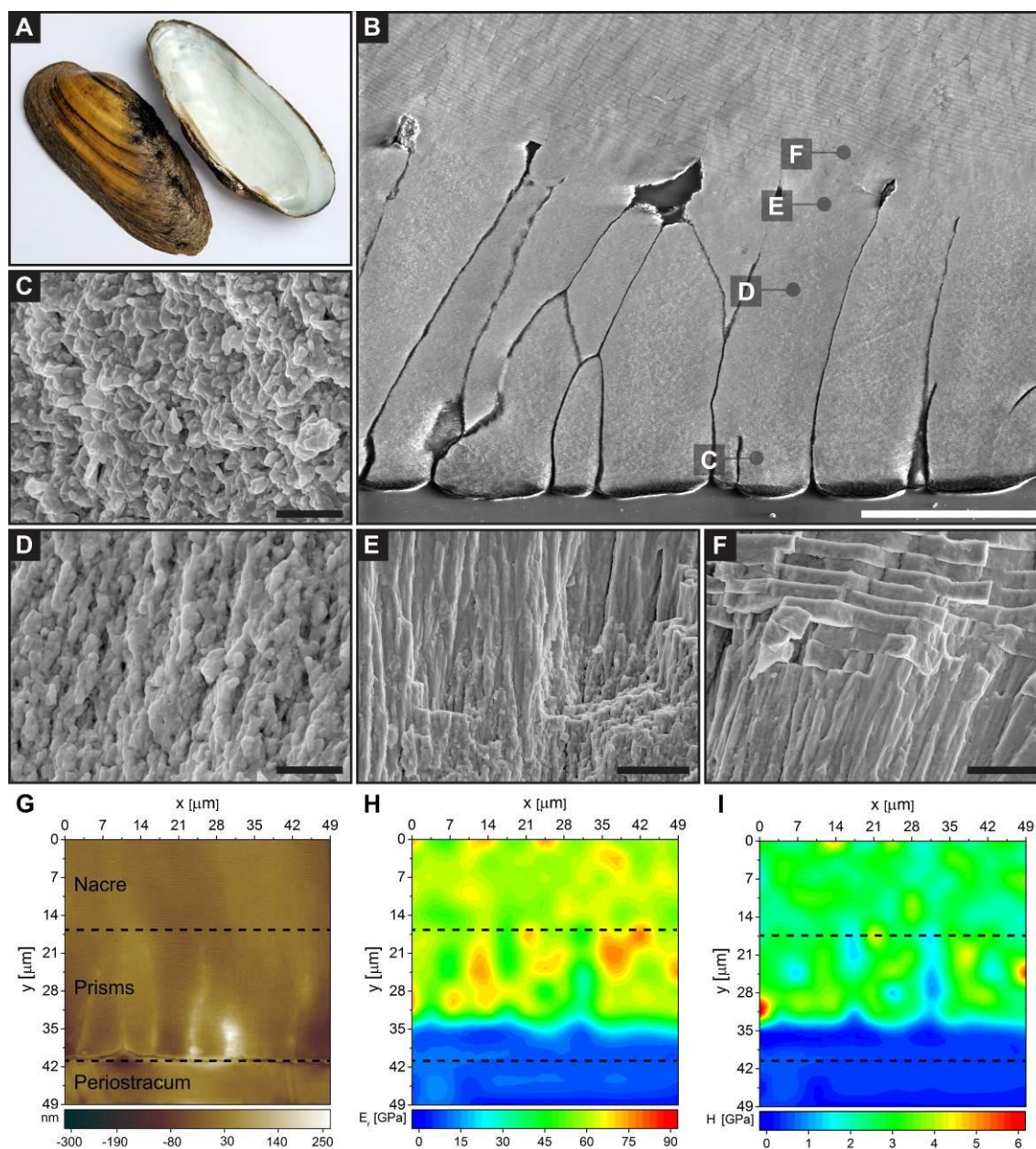


Figure 1. Nanostructural and mechanical properties of the shell of *U. pictorum*. A) Two valves of the shell with the exposed periostracum (left) and exposed nacreous layer (right). B) ESEM image of a polished cross-section prepared perpendicular to the surface of the shell. The scale bar is 50 μm . C-F) SEM images of a cryo-fractured cross-section of the shell taken from areas indicated in B. Scale bars are 1 μm , 1 μm , 3 μm , and 3 μm , respectively. G) Topography of a cross-section of the shell prepared perpendicular to its outer surface. H-I) Reduced modulus and hardness maps of the area in (G) measured by nanoindentation, respectively.

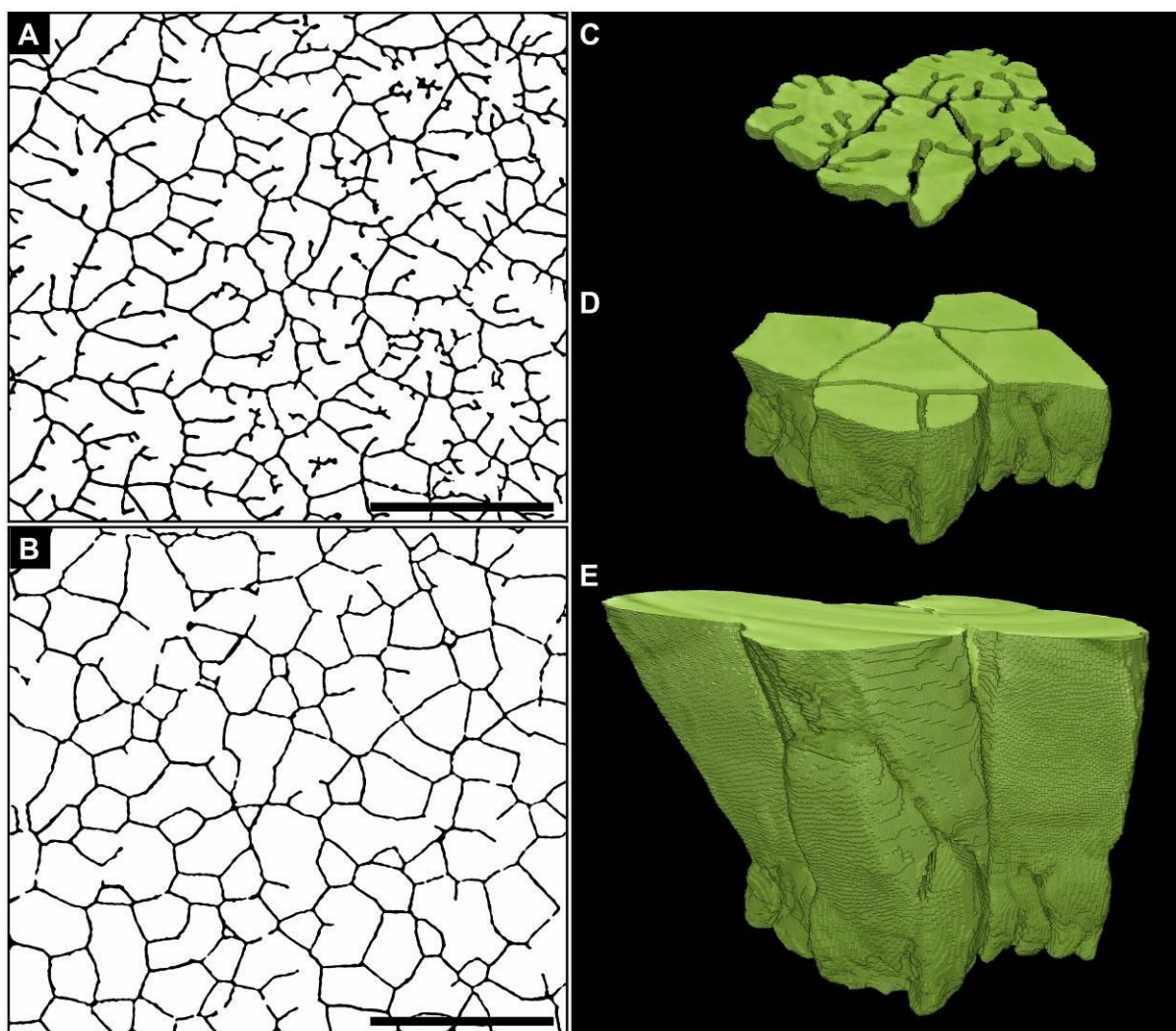


Figure 2. Morphological analysis of the dendritic-prismatic ultrastructure in the shell of *U. pictorum*. A-B) 2D slices reconstructed from synchrotron-based microtomography data, (parallel to the surface of the shell), showing the dendritic and the prismatic morphology, closer to the periostracum and nacre, respectively. White areas correspond to the mineral component, and black areas to the organic phase. Scale bars are 100 μm . C-E) 3D visualization of tomographic segments showing different stages of structural evolution of the dendritic-prismatic ultrastructure: initial stage showing the dendritic morphology, intermediate stage showing transition to the prismatic morphology and the complete ultrastructure, respectively.

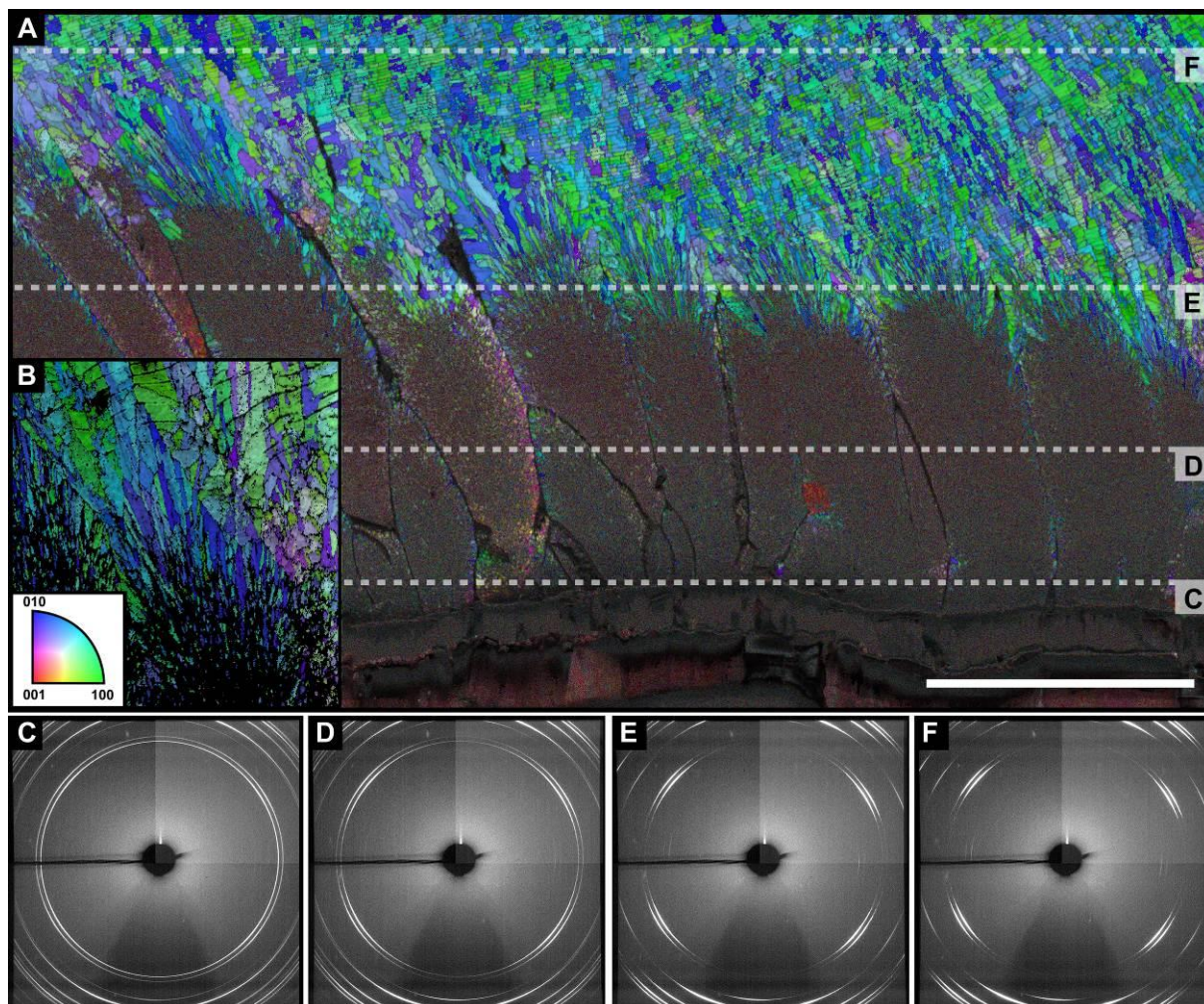


Figure 3. Crystallographic analysis of the shell of *U. pictorum*. A) EBSD map of a polished cross-section perpendicular to the shell's surface. Scale bar is 100 μm . B) Magnified EBSD map of the transition between the prismatic and the nacreous ultrastructures. The corresponding inverse pole figure is color-coded along the specimen normal which is the direction pointing towards the viewer. The blue-green coloring indicates that the (100) and (010) plane normals of aragonite are oriented horizontally in the shell structure while the (001) plane normal is vertical along the growth direction of the shell. C-F) X-ray diffraction patterns collected at different positions in the shell. Measured locations are indicated as dashed lines in (A).

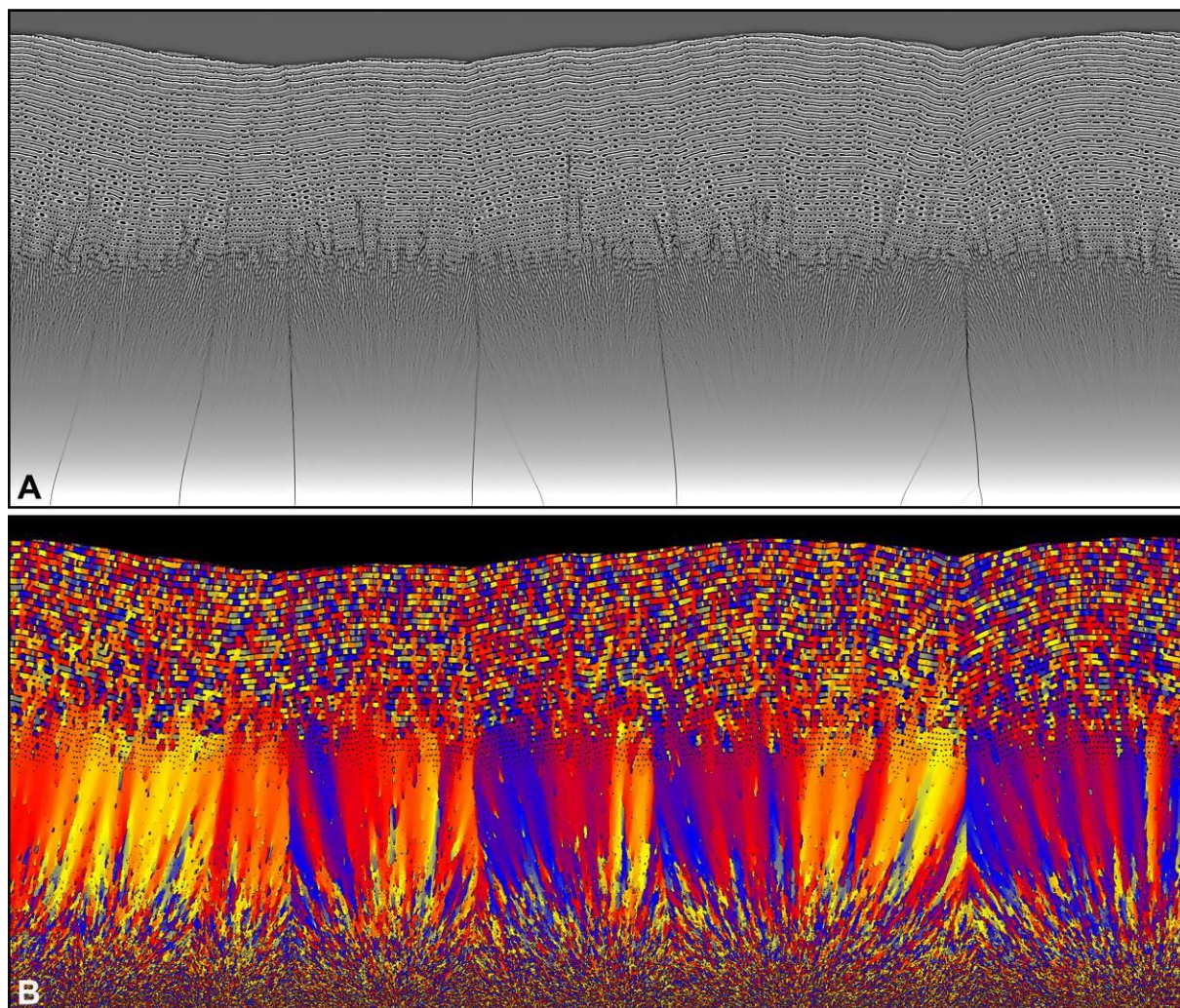


Figure 4. Shell morphology as predicted by two-dimensional phase-field simulation under decreasing supersaturation. A) Concentration map: light gray – calcium carbonate rich, dark gray – organic-component-rich. Note that the prisms are formed from eight nucleation events: the borders between such areas are indicated by lines of organic-component-rich solid. B) Orientation map: black – fluid, different colors stand for different crystallographic orientations.